Canted antiferromagnetic order and spin dynamics in the honeycomb-lattice compound $Tb_2Ir_3Ga_9$

Feng Ye,[1,*] Zachary Morgan,[1] Wei Tian,[1] Songxue Chi,[1] Xiaoping Wang,[1] Michael E. Manley,[2] David Parker,[2] Mojammel A. Khan,[3,†] J. F. Mitchell,[3] and Randy Fishman[2,‡]

[1]*Neutron Scattering Division, Oak Ridge National Laboratory, Oak Ridge, Tennessee 37831, USA*

[2]*Materials Science and Technology Division, Oak Ridge National Laboratory, Oak Ridge, Tennessee 37831, USA*

[3]*Materials Science Division, Argonne National Laboratory, 9700 South Cass Avenue, Argonne, Illinois 60439, USA*

(Received 3 March 2021; accepted 19 April 2021; published 12 May 2021)

Single-crystal neutron diffraction, inelastic neutron scattering, bulk magnetization measurements, and first-principles calculations are used to investigate the magnetic properties of the honeycomb lattice $Tb_2Ir_3Ga_9$. While the $R\ln 2$ magnetic contribution to the low-temperature entropy indicates a $J_{\rm eff} = 1/2$ moment for the lowest-energy crystal-field doublet, the Tb^{3+} ions form a canted antiferromagnetic structure below 12.5 K. Due to the Dzyaloshinskii-Moriya interactions, the Tb moments in the *ab* plane are slightly canted towards **b** with a canted moment of 1.22 μ_B per formula unit. A minimal *xxz* spin Hamiltonian is used to simultaneously fit the spin-wave frequencies along the high-symmetry directions and the field dependence of the magnetization along the three crystallographic axes. Long-range magnetic interactions for both in-plane and out-of-plane couplings up to the second nearest neighbors are needed to account for the observed static and dynamic properties. The z component of the exchange interactions between Tb moments is larger than the x and y components. This compound also exhibits bond-dependent exchange with negligible nearest-neighbor exchange coupling between moments parallel and perpendicular to the $4f$ orbitals. Despite the $J_{\rm eff} = 1/2$ moments, the spin Hamiltonian is denominated by a large in-plane anisotropy $K_z \sim -1$ meV. DFT calculations confirm the antiferromagnetic ground state and the substantial interplane coupling at larger Tb-Tb distances.

DOI: 10.1103/PhysRevB.103.184413

I. INTRODUCTION

Materials that support a quantum spin liquid (SL) state are of great interest in condensed-matter physics. On the honeycomb lattice, it is well known that the Kitaev model produces various two-dimensional topological SL states [1–3]. Bond-directional anisotropic exchange on a honeycomb lattice frustrates simple collinear magnetic order [1,4] in $4d$ and $5d$ transition-metal candidates such as α-$RuCl_3$ [5,6] and A_2IrO_3 (A = Li, Na) [4,7,8], where strong spin-orbit coupling (SOC) produces $J_{\rm eff} = 1/2$ moments. These systems underscore the recent interest in the honeycomb structural motif.

Decorating the honeycomb lattice with rare-earth ions offers an alternative to $4d$- and $5d$-based materials. For example, $YbMgGaO_4$, $YbCl_3$, and $TbInO_3$ are proposed quantum SL candidates [9–12] with $J_{\rm eff} = 1/2$. Recent theoretical treatments of SOC entanglement in rare-earth honeycomb magnets motivates further exploration of similar systems [13,14].

A nearly ideal honeycomb lattice of rare-earth ions occurs in the family $R_2T_3X_9$, where R is a rare-earth element, T is a transition-metal element, and X is a p-block element. Occupying a large composition space, this family hosts a rich phenomenology, including complex magnetic order for Dy-based compounds [15], mixed valence in Yb/Ce-based compounds [16–18], and Kondo-lattice behavior for the Yb-based compounds [19,20].

With an orthorhombic crystal structure of the $Y_2Co_3Ga_9$ type [21–23] (space group No. 63, *Cmcm*), $Tb_2Ir_3Ga_9$ (TIG) contains alternating $IrGa_2$ (A) and Tb_2Ga_3 (B) layers. Along **c**, these layers stack to form an A-B-A'-B' sequence, where layers A' and B' result from a mirror-plane operation on layers A and B. The magnetic Tb atoms form a slightly distorted honeycomb network, with two short Tb-Tb bonds of 4.28 Å along **a** and four longer bonds of 4.38 Å rotated approximately $\pm 60^\circ$ away from **a** [Fig. 1].

The crystal field splits the 13-fold degenerate $L = 3$, $S = 3$, and $J = 6$ levels of Tb^{3+} into a low-lying non-Kramers or "pseudo" doublet [24,25] and 11 higher levels. Due to the interactions between ions, this low-lying doublet hybridizes with a higher-energy doublet. Since the resulting hybridized doublet has nonzero matrix elements of J_{iz} and $J_{i\pm}$ with respect to the Ising axis, the magnetic Tb^{3+} moments can be treated as $J_{\rm eff} = 1/2$ moments.

Hexagon-shaped single crystals of TIG, with a typical size of a few millimeters (mm) on the edge and 1–2 mm in thickness, were grown at Argonne National Laboratory using a Ga-flux method [26]. The magnetization was measured using a Quantum Design SQUID. Neutron diffraction was performed on the HB1A triple axis spectrometer at the High Flux Isotope Reactor (HFIR) and on the CORELLI and TOPAZ diffractometers at the Spallation Neutron Source, all

*yef1@ornl.gov

†Present address: Department of Physics and Astronomy and Department of Chemistry, Johns Hopkins University, Baltimore, Maryland 21218, USA.

‡fishmanrs@ornl.gov

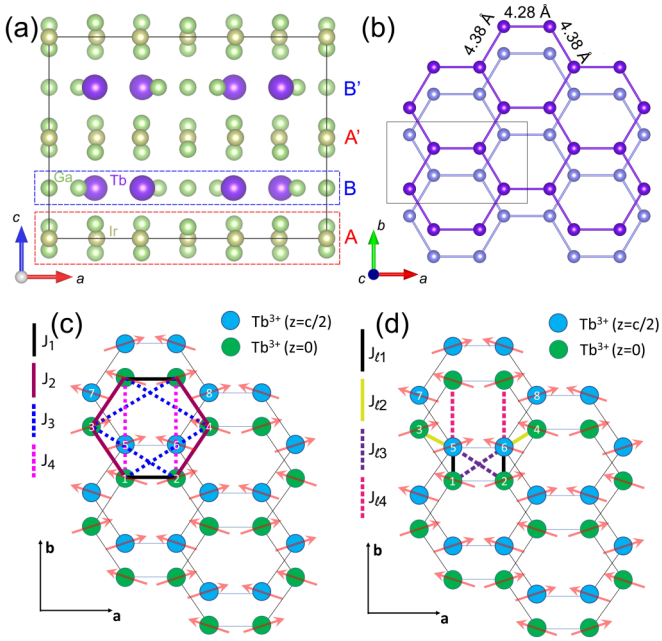

FIG. 1. (a) The crystal structure of TIG projected onto the *ac* plane. The structure is composed of stacked $(AB)_2$ layers, where A is a buckled $IrGa_2$ layer (Ir atoms form a triangle lattice), and B is a Tb_2Ga_3 layer (Tb atoms form a pseudohoneycomb lattice). (b) The network of Tb ions viewed from the **c** axis. The black rectangular box in panels (a) and (b) is the unit cell. (c), (d) The canted AFM spin configuration with magnetic space group $Cm'cm'$. J_1, J_2, J_3, and J_4 are the in-plane exchange interactions with Tb-Tb distances of 4.28, 4.38, 7.52, and 7.54 Å, respectively; J_{l1}, J_{l2}, J_{l3}, and J_{l4} are the interlayer exchange interactions with Tb-Tb distances of 5.36, 5.37, 6.86, and 6.89 Å, respectively, all at room temperature.

at the Oak Ridge National Laboratory (ORNL). Diffraction studies were made on a naturally cleaved single crystal with dimensions $2 \times 2 \times 1$ mm^3. Sample temperature T was controlled by using the orange cryostat at HB1A, closed-cycle refrigerator (CCR) at CORELLI, and Cryomech P415 pulse tube cryocooler at TOPAZ.

Inelastic neutron scattering (INS) studies were performed on the HB1 and HB3 triple-axis spectrometers at the HFIR. A sample assembly of 36 single crystals (total mass ≈3.4 g, mosaicity ≈1.5°) was aligned in the $(H, 0, L)$ scattering plane to probe magnetic excitations in the basal plane and between layers. Due to the weak orthorhombic distortion, no attempt was made to align the pseudohexagonal crystals along their common orthorhombic axis **a**. A CCR was used to regulate the temperature for the INS measurements at HB1 and HB3.

The absence of a detectable signal from x-ray magnetic circular dichroism (XMCD) measurements at the Ir L edges places the upper limit for the Ir moments at 0.01 μ_B [26]. In the same work, the refined neutron powder diffraction pattern indicated that the Tb spin configuration can best be described as collinear order in the basal plane with easy axis along **a**, consistent with the magnetic space group (MSG) $Cm'cm'$. Although canted antiferromagnetic (AFM) order is allowed by this MSG [Figs. 1(c) and 1(d)], introducing a ferromagnetic (FM) component along **b** did not improve the refinement.

Analysis of the magnetic properties is simplified by the confinement of the magnetic moments to the Tb sites [26]. Under an applied field along **a**, the magnetization $M_a(H)$ shows step-like transitions at 2.5 and 6.5 T. With increasing field along **c**, $M_c(H)$ exhibits a linear response. While the **b**-axis magnetization M_b shows a similar linear behavior, the hysteresis loop below 1 T indicates the presence of a FM component.

The nearly Ising character of the Tb moments was demonstrated by measurements of the critical fields B_{c1} and B_{c2} as the field is rotated by an angle ϕ away from the **a** axis within the ab plane. Both $B_{c1}(\phi)\cos\phi$ and $B_{c2}(\phi)\cos\phi$ are almost independent of angle ϕ up to about $\pi/3$. Therefore, the component of the field along the **a** axis predominantly controls the magnetic phase transitions [26]. Similar results were found for the Ising-like compounds $TbNi_2Ge_2$ [27] and $Y_{1-x}Tb_xNi_2Ge_2$ [28], where the Ni atoms are nonmagnetic because the Stoner criteria is not satisfied [29].

II. NEUTRON-DIFFRACTION RESULTS

Although the two-dimensional (2D) spin Hamiltonian employed in an earlier study [26] captured the key characteristics of the exchange interactions and described the metamagnetic transitions, the magnetic order derived from neutron powder diffraction is clearly three dimensional (3D). However, the sizable Dzyaloshinskii-Moriya (DM) interaction that produces the FM moment along **b** was not observed in neutron powder diffraction. To reconcile this inconsistency, a comprehensive study of the static spin order and magnetic dynamics using single crystals was undertaken.

We first investigated the static magnetic order at low temperature. Figure 2(a) provides a contour plot of the neutron-diffraction data in the $(H, 0, L)$ scattering plane at 7 K measured at CORELLI [30]. Consistent with neutron powder diffraction, all observed reflections lie at integer indices, indicating that the magnetic peaks coincide with the nuclear ones and have a propagation wave vector (0,0,0). Group theory analysis indicates that the magnetic representation for the Tb ion located at (0.336, 0.332, 1/4) can be decomposed into a summation of four one-dimensional (1D) irreducible representations (IRs) with moment only allowed along the **c** axis and four two-dimensional IRs with a moment permitted in both the **a** and **b** directions [26]. Since the magnetization reveals a prevailing in-plane moment, the 1D IRs with **c**-axis moment were not used to refine the magnetic structure. A mapping of the 3D reciprocal volume at the CORELLI diffractometer at 7 K yields 393 reflections that contain both magnetic and nuclear contributions. Simultaneously fitting both the crystal and magnetic structures reveals a canted AFM structure best described by magnetic space group $Cm'cm'$. Details are given in the Supplemental Material [31]. In contrast with results of neutron powder diffraction, this single-crystal study identifies a small FM component along **b**.

Confirming this FM moment, Fig. 2(b) plots the thermal evolution of the (0,0,2) peak collected by using a fixed incident energy at the triple-axis spectrometer HB1A. If canted order were absent, this reflection would be T independent. Albeit weak, the abrupt enhancement (about 4%) below

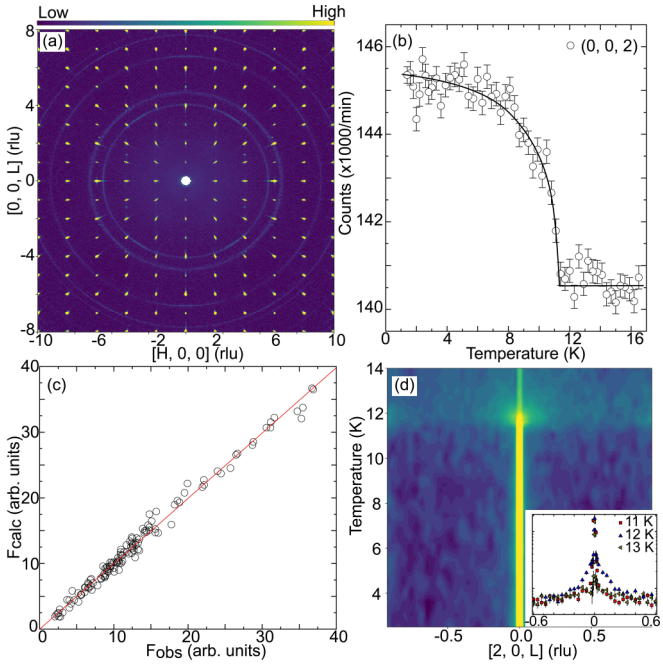

FIG. 2. (a) Contour plot of the neutron-diffraction data in the $(H, 0, L)$ scattering plane collected on CORELLI at $T = 7$ K. (b) T dependence of the (0,0,2) Bragg peak measured at HB1A. The solid line is a guide to the eye. (c) Comparison between the observed and calculated structure factors, $F_{\rm obs}$ and $F_{\rm calc}$. The (red) line is a linear fit to the data points. (d) The T dependence of the L scan across the (2,0,0) Bragg point. The inset shows the representative line cut along the $[0, 0, L]$ direction at 11, 12, and 13 K, with prominent short-range correlation at 12 K.

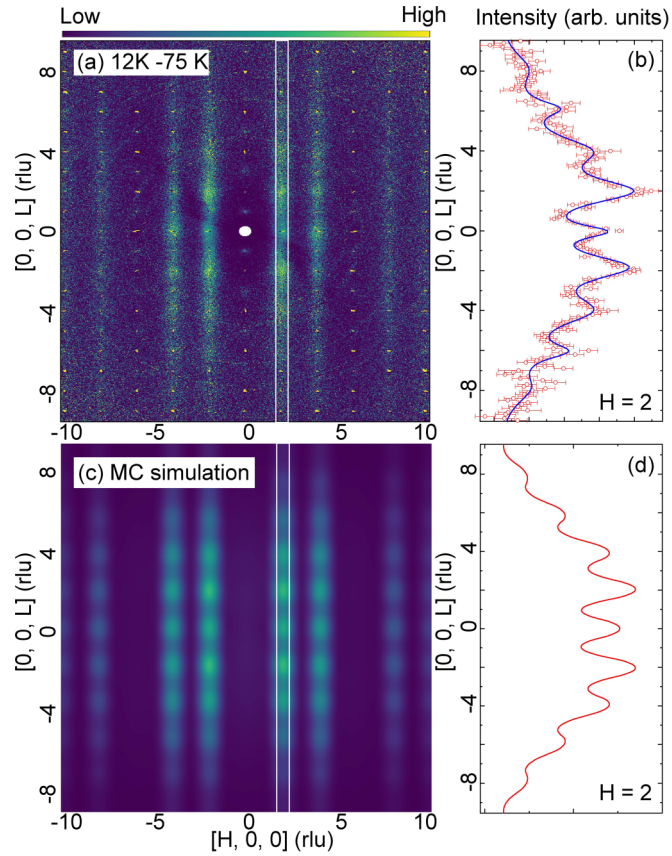

FIG. 3. (a) Contour plot of the neutron-diffraction data in the $(H, 0, L)$ scattering plane. A rod-like feature along $[0, 0, L]$ indicates the short-range magnetic correlations along the **c** axis. (b) For the line cut along $[2, 0, L]$, Lorentzian profiles appear at even indices. (c) Monte Carlo simulation of the magnetic diffuse scattering just above the transition using the magnetic exchange parameters in Table I. (d) The corresponding line cut along $[2, 0, L]$.

$T_{\rm N}$ confirms the FM component along **b**. Summarized in Figs. 1(c) and 1(d), the Tb moments form a predominantly AFM state along **a** canted by 6.7(3)° towards **b**. This produces 2.06 $\mu_{\rm B}$/f.u. along **b**, which is somewhat larger than the value obtained from magnetization measurements of 1.22 $\mu_{\rm B}$/f.u. The ordered moment along **a** is 17.8(4) $\mu_{\rm B}$ per formula unit (f.u.), in excellent agreement with magnetization measurements.

Since the Tb atoms form an orthorhombic rather than a true honeycomb lattice, the collected single crystal diffraction data comprise three unevenly populated structural and magnetic domains. The refinement on a single piece of the crystal yields a domain volume fraction ratio of 11 : 77 : 12. These three domains are described by rotation matrices: the first corresponds to the crystal orientation matrix and the other two are given by rotations of ±60° about **c**. The coexistence of those twinned domains explains the strong magnetic Bragg reflections, such as $(2, 0, L = 2n)$. An independent measurement at the TOPAZ diffractometer on the same single crystal at 9.6 K (closer to the transition) confirms the refinement results for the canted spin configuration.

Notably, the single-crystal study indicates a significant magnetic correlation between honeycomb layers just above T_N, as shown by the T dependence of the L scan across $(2, 0, L)$ [Fig. 2(d)]. A more detailed characterization of the spin-spin correlation is given by the $(H, 0, L)$ slice in Fig. 3(a), which shows the $T = 12.5$ K data after the 75 K data are subtracted as background. Short-range spin fluctuations along $[0, 0, L]$ are prominent at $H = -8$, -4, -2, 2, 4, and 8. The 1D line cut at $H = 2$ with $\Delta H = \pm 0.2$ shown in Fig. 3(b) can be fit as the summation of multiple Lorentzian profiles peaked at $L = 2n$ on top of a broad Lorentzian background. The half width half maximum (HWHM) of these profiles ranges from 0.60 to 0.98 reciprocal-lattice units (rlu), corresponding to a magnetic correlation length from 9.6 to 15.8 Å, which is longer than the nearest-neighbor Tb-Tb distances (≈5.4 Å) between honeycomb layers. Whereas the magnetic diffuse scattering in pure 2D systems should exhibit featureless fluctuations between the layers, the observed multiple peaks indicate considerable 3D magnetic correlations along **c** and are consistent with the spin dynamics analysis presented below.

III. INELASTIC-NEUTRON-SCATTERING STUDY

Figures 4(a)–4(c) show the spin-wave spectra measured at base temperature along three high-symmetry directions $[\xi, 0, 3]$, $[\eta, 0, 4 - \eta]$, and $[0, 0, L]$. The data are obtained through energy scan at fixed momentum transfer with an energy step of $\Delta E = 0.25$ meV. A Gaussian profile is used

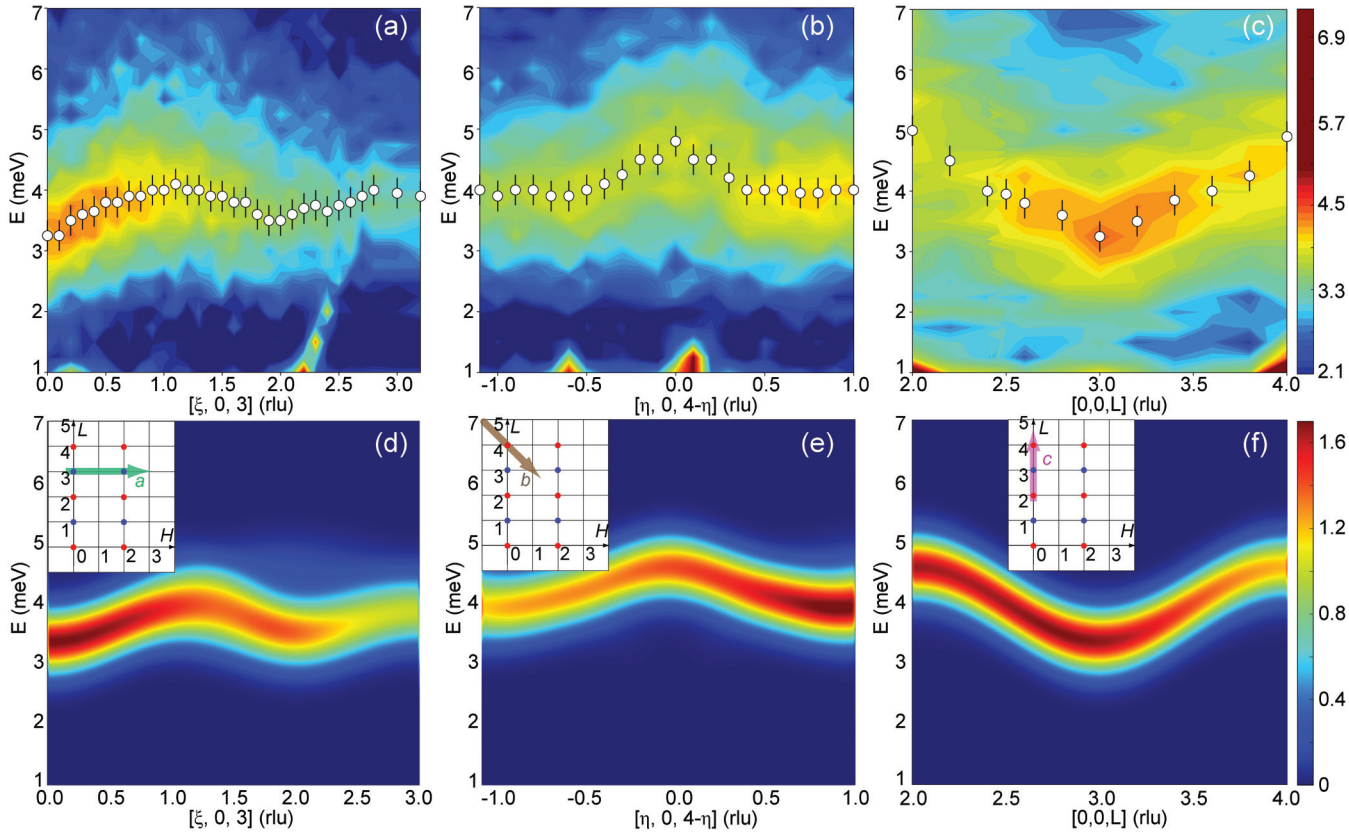

FIG. 4. SW dispersion spectra of $Tb_2Ir_3Ga_9$ along (a) $[\xi, 0, 3]$, (b) $[\eta, 0, 4-\eta]$, and (c) $[0, 0, L]$. The corresponding calculated spectra are shown in panels (d)–(f). Individual scans at constant moment transfer are measured from $E = 1$ to 7 meV with step of 0.25 meV. The solid circles in panels (a)–(c) specify the measured momentum transfer. Insets show the schematics of the scan directions in the $(H, 0, L)$ scattering plane. In untwinned samples, only red dots are allowed Bragg reflections $(H, L = 2n)$, the blue dots represent the observed Bragg peaks contributed from twinned domains, as shown in Fig. 2(a). The dispersion-like feature for energy transfer below 3 meV in panel (a) arises from the tail of the resolution function sweeping through the neighboring Bragg peak in the focusing geometry.

to obtain the peak position of the individual scan. The spin excitations clearly exhibit momentum dependence in all plots indicating the exchange interactions are three dimensional.

An earlier description [26] of TIG was based on a model with anisotropic exchange along the bond direction $\mathbf{R}_i - \mathbf{R}_j$ between Tb^{3+} ions in each layer. That model provided an excellent description of the magnetization data. However, as discussed further below, it does not provide an adequate description of the spin dynamics. Therefore, we now study TIG using an xxz model, which has been previously used to describe other layered honeycomb systems [32–34] and has also been proposed for rare-earth compounds [35]. The Hamiltonian is given by

$$\begin{aligned}\mathcal{H} = &-\frac{1}{2}\sum_{i,j} J_{ij}^{xy}\{S_{ix}S_{jx} + S_{iy}S_{jy}\} - \frac{1}{2}\sum_{i,j} J_{ij}^{z} S_{iz}S_{jz} \\ &-\frac{1}{2}\sum_{i,j} J_{lij}^{xy}\{S_{ix}S_{jx} + S_{iy}S_{jy}\} - \frac{1}{2}\sum_{i,j} J_{lij}^{z} S_{iz}S_{jz} \\ &- K_x\sum_i S_{ix}^2 - K_z\sum_i S_{iz}^2 - \frac{1}{2}\sum_{i,j}^{1\text{st, }2\text{nd}} \mathbf{D}_{ij}\cdot(\mathbf{S}_i \times \mathbf{S}_j) \\ &- \mu_B\sum_{i,\alpha} g_{\alpha\alpha}B_\alpha S_{i\alpha}, \end{aligned} \tag{1}$$

which replaces the total angular momentum $\mathbf{J_i}$ of Tb^{3+} by an effective spin $\mathbf{S_i}$ at site i. Exchanges J_n act between spins within each ab plane and exchanges J_{ln} act between spins on neighboring planes [Figs. 1(c) and 1(d)]. Each exchange interaction contains an xy part J_{ij}^{xy} that couples the x and y components of the spin and a z part J_{ij}^{z} that couples the z-spin components.

Although single-ion anisotropy is expected to vanish within the $J_{\text{eff}} = 1/2$, non-Kramers or "pseudo" doublet state of Tb^{3+} [24,25], easy-plane and easy-axis anisotropies K_z and K_x confine the spins in the basal plane and align them along $\mathbf{a}$. These single-ion anisotropy terms will be further discussed in the conclusion.

While the nominal g factor for $S = L = 3$ and $J = 6$ moments is $g = 3/2$, we treat the diagonal components g_{xx}, g_{yy}, and g_{zz} of the g tensor as fitting parameters, multiplied by B_α, the α-component of the field. Initial fitting results indicated that the nearest-neighbor interactions (both xy and z components) J_1 and J_{l1} can be set to zero. The z components of J_3, J_4, and J_{l4} are small and neglected. It is permissible to take $J_3^{xy} = J_4^{xy}$, which is expected from the nearly identical distances 7.52 and 7.54 Å spanned by those interactions.

The DM interaction $\mathbf{D}_{ij} = D\mathbf{c}$ is allowed by the broken inversion symmetry caused by the alternation of the Ir^{4+} ions on either side of the Tb-Tb bond moving around a hexagon

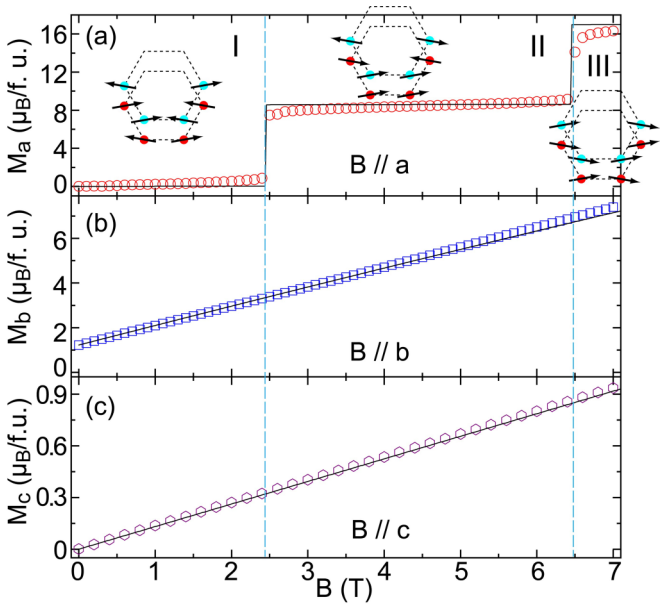

FIG. 5. Magnetization $M(H)$ with field applied along the three crystallographic axes up to 7 T at 1.8 K. Open symbols are experimental data; solid lines are the best fits described in the text. The spin configurations in three distinct region with field $B \parallel \mathbf{a}$ are sketched in panel (a).

in the honeycomb lattice. This DM interaction couples both nearest-neighbor spins 1 and 2 or 3 and 4 separated by 4.28 Å, and next-nearest-neighbor spins 1 and 3 or 2 and 4 separated by 4.38 Å. Whereas D cants the spins away from the **a** axis, the exchange interactions and the easy-axis anisotropy K_x favor a collinear state. Minimizing the total energy, the canting angle is given by

$$\theta = \frac{1}{2}\tan^{-1}\left\{\frac{3D}{J_1 + 2J_2 + 2J_{l1} + 2J_{l4} - K_x}\right\}. \quad (2)$$

Since $M_0 = 2g_{yy}\mu_B S\sin\theta \approx 1.22\ \mu_B$ is the canted moment per f.u. along **b** observed by magnetization measurements [Fig. 5(b)], Eq. (2) fixes D in terms of the other model parameters and M_0. Hence, the total of fitting parameters is 13 (Table I).

Even though neutron-diffraction measurement on one single crystal revealed an uneven distribution of domains, we made no effort to align the orthorhombic axes of the 36 small crystals. Due to the large number of single crystals, we expect an equal fraction of those crystals to have their orthorhombic axes along (1,0,0), $(1/2, \sqrt{3}/2, 0)$, and $(-1/2, \sqrt{3}/2, 0)$ for domains 1, 2, and 3, respectively. This is confirmed by a least-squares fit of the corresponding domain contributions to the magnetic peak intensities. For scans along (H, K, L) with $K = 0$, domains 2 and 3 have the same set of SW branches but domain 1 has a different set.

The SW dynamics at zero field is evaluated by taking sites 1 and 4 (5 and 8) and sites 2 and 3 (6 and 7) on layer 1 (2) to be identical. Since the magnetic unit cell contains four distinct spins, each domain produces four SW modes. For scans along $(\xi, 0, 3)$ and $(\eta, 0, 4-\eta)$, our model predicts eight SW branches. For the scan along $(0, 0, L)$, each domain produces the same spectra and our model predicts four SW branches.

However, Figs. 4(a)–4(c) reveal a single wide SW branch for each scan. To compare the calculated and measured SW frequencies, we perform a weighted average over the calculated frequencies at each wave vector:

$$\omega_{\rm av}(\mathbf{q}) = \frac{\sum_n \omega_n(\mathbf{q}) S_n(\mathbf{q})}{\sum_n S_n(\mathbf{q})}, \quad (3)$$

where the weight $S_n(\mathbf{q})$ is obtained from the spin-spin correlation function $S_{\alpha\beta}(\mathbf{q}, \omega)$ using

$$S(\mathbf{q}, \omega) = \left\{\delta_{\alpha\beta} - \frac{q_\alpha q_\beta}{q^2}\right\} S_{\alpha\beta}(\mathbf{q}, \omega) = \sum_n S_n(\mathbf{q})\delta(\omega - \omega_n(\mathbf{q})). \quad (4)$$

To order $1/S$ in the Holstein-Primakoff expansion [36], each mode produces a δ function $\delta(\omega - \omega_n(\mathbf{q}))$ with weight $S_n(\mathbf{q})$.

Our original fits based solely on the weighted SW frequencies produced a wide spread in SW intensities that was inconsistent with the measurements. Therefore, we constrained the observed spread in frequencies to be greater than or equal to the calculated spread $2\Delta\omega(\mathbf{q})$, where

$$\Delta\omega(\mathbf{q})^2 = \frac{\sum_n [\omega_n(\mathbf{q}) - \omega_{\rm av}(\mathbf{q})]^2 S_n(\mathbf{q})}{\sum_n S_n(\mathbf{q})}. \quad (5)$$

The cost function in $\chi^2_{\rm INS}$ used an experimental uncertainty in the peak SW frequencies of $\sigma_\omega = 0.25$ meV for both instruments HB1 and HB3.

To evaluate the magnetic $\chi^2_{\rm mag}$, we used an experimental uncertainty in the magnetization of ±6% for a field above B_{c1} along **a** and for all fields along **b** and **c**. The calculated critical fields B_{c1} and B_{c2} along **a** were constrained to agree with the measured critical fields. In addition, $B_{cn}(\phi)\cos\phi$ was constrained to be nearly independent of the angle ϕ between the applied field and the **a** axis within the ab plane up to

TABLE I. The in-plane and out-of-plane exchange interaction parameters J_i and J_{li}, easy-axis and easy-plane anisotropies K_x and K_z and DM exchange interaction D, units in meV. Values in parentheses are one standard deviation.

Parameter	Value	
	xy	z
J_1	0	0
J_2	−0.016(2)	−0.05(2)
$J_3 = J_4$	0.007(1)	0
J_{l1}	0	0
J_{l2}	−0.027(2)	0.09(2)
J_{l3}	0.014(6)	−0.16(6)
J_{l4}	−0.014(2)	0
K_x	0.09(1)	
K_z	−0.84(6)	
D	−0.0066	
g_{xx}	1.38(1)	
g_{yy}	1.51(3)	
g_{zz}	1.59(6)	

$\phi = \pi/3$. The 13 fitting parameters were then determined by minimizing $\chi^2 = \chi^2_{\rm mag} + \chi^2_{\rm INS}$.

IV. FITTING RESULTS

To compute the spectra, the δ-function intensities $S_n(\mathbf{q})\delta(\omega - \omega_n(\mathbf{q}))$ were convoluted over a Lorentzian with width $\nu = 0.5$ meV, which is close to the instrumental resolution for both HB1 and HB3, and then multiplied by the square of the magnetic form factor $f(q)$ for Tb^{3+}. Results for the calculated magnetization and inelastic intensities are plotted in Figs. 5(a)–5(c) and in Figs. 4(d)–4(f), respectively. These results are quite satisfactory with a few reservations. First, the calculated intensity along $[\xi, 0, 3]$ is fairly large up to $\xi = 3$, while the observed intensity drops off rapidly above $\xi = 2$. Second, the calculated intensity along $[0, 0, L]$ peaks to the left of $L = 3$ while the observed intensity peaks to the right. Third, the calculated magnetization is slightly too small for fields along **b** and **c** in Figs. 5(b) and 5(c). By contrast, the calculated magnetization for field along **a** in Fig. 5(a) is slightly too large in the plateau between 2.5 and 6.5 T.

The microscopic parameters that minimize the total χ^2 are given in Table I. The resulting g tensor parameters have an average value $g_{\rm av} = (g_{xx} + g_{yy} + g_{zz})/3$ of 1.50(3), consistent with the nominal $J = 6$ value of $g = 1.5$. This result is consistent with measurements [26] of the Curie-Weiss susceptibility, which gives an effective moment of 10.3 $\mu_{\rm B}$/Tb, close to the free-ion value of 9.7 $\mu_{\rm B}$/Tb when $g = 1.5$.

By far the largest energy among the fitting parameters is the easy-plane anisotropy $K_z \approx -0.83$ meV. A rough estimate for K_z can be obtained from the observed magnetization when a field is applied along **c**. Neglecting the exchange interactions, the energy per spin is given by

$$E = K_z S^2 \cos^2\theta - \mu_{\rm B} g H S \sin\theta, \tag{6}$$

where θ is the canting angle of the spin towards **c**. Minimizing this energy with respect to θ gives a magnetization per f.u. of

$$M_z = 2 g_{zz} \mu_{\rm B} S \sin\theta = \frac{\mu_{\rm B}^2 g^2 H}{|K_z|}. \tag{7}$$

Using the experimental result $M_z = 0.94$ $\mu_{\rm B}$/f.u. at 7 T (corresponding to a tilt angle of $\theta = 3.1^\circ$) and the value $g_{zz} = 1.59$ from Table I, we find $K_z \approx -0.98$ meV (a value of -0.88 meV was found in Ref. [26]). Thus, a large value of K_z is required to explain the small magnetization when a field is applied along **c**. For bulk Tb in a hexagonal close-packed structure, Rhyne *et al.* [37] reported a tilt angle of 8.6° in a 7 T field, corresponding to $K_z \approx -0.32$ meV, less than half the size of that reported here. A similar analysis based on the change in magnetization of 6.2 $\mu_{\rm B}$/f.u. in a 7 T field along the **b** yields $K_x \approx 0.13$ meV, which is larger than our fitting result 0.09 meV because the xy exchange energy also strongly favors an AFM state.

Another remarkable feature of these results is that the z exchange couplings are substantially larger than the xy couplings. To gain further insight, we minimized $\chi^2_{\rm mag}$ without any dynamical contribution with respect to the same five xy exchange parameters and two anisotropies: $J_2^{xy} = -0.014$, $J_3^{xy} = 0.007$, $J_{l2}^{xy} = -0.027$, $J_{l3}^{xy} = 0.014$, $J_{l4}^{xy} = -0.016$, $K_x = 0.08$, and $K_z = -0.84$, all in meV. Note that this model is still three dimensional because it contains interactions between layers as well as easy-plane anisotropy. This static fit also gives $g_{xx} = 1.39$, and $g_{yy} = g_{zz} = 1.49$. While $\chi^2_{\rm mag}$ slightly decreases from 0.30 for the xxz model with dynamical input to 0.29 for the xx model without dynamical input, the resulting xy exchange parameters are close to those obtained in Table I from fitting the full $\chi^2 = \chi^2_{\rm mag} + \chi^2_{\rm INS}$. Hence, the z-exchange couplings are *not* required to explain the magnetization measurements.

The earlier model in Ref. [26] used eight parameters to explain the magnetization, fixing $g = 1.5$ but adding hexagonal anisotropy. By comparison, the model described above uses ten parameters, including $g_{\alpha\alpha}$ but neglecting hexagonal anisotropy. In both models, the exchange between spins 1 and 3 or 2 and 4 along a side of the hexagon is greater than the exchange between spins 1 and 2 or 3 and 4 along the top or bottom of the hexagon. Hence, bond-dependent exchange is required to understand the magnetization measurements of TIG.

Assuming now that the exchange interactions are isotropic ($J_{ij}^{xy} = J_{ij}^{z}$), minimizing the total χ^2 with respect to all eight exchange parameters gives $\chi^2 = 0.65$, which is greater than the value 0.33 obtained using the *anisotropic* parameters in Table I. Hence, the five large z exchange components in Table I are required to explain the inelastic measurements. Using a fitting technique that constrains the frequency width of the inelastic spectra, we believe that our model contains the minimum number of parameters that can adequately describe TIG.

The fitting result $g_{xx} = 1.38(1)$ gives the saturation magnetization 16.5(2) $\mu_{\rm B}$/f.u. and the ordered moment of 8.3(1) $\mu_{\rm B}$ for field along **a**. For comparison, the ordered moment 8.9(2) $\mu_{\rm B}$ obtained from neutron-diffraction measurements gives $g = 1.48(3)$.

Using the parameters in Table I, we have also evaluated the predicted spectra at the two plateaus of the magnetization for regions II and III in Fig. 5(a). It should be easy to observe the changes in the inelastic spectra compared with the spectra at zero field. The predicted spectra for a 7 T field along **a** (for domain 1 only) in region III is shown in Fig. 2 of the Supplemental Material [31].

As an additional check on our results, we compare the observed [26] transition temperature of 12.5 K with the mean-field (MF) Néel temperature evaluated for Ising spins:

$$T_{\rm N}^{\rm MF} = z|J_{xy}|\frac{S(S+1)}{3}, \tag{8}$$

where

$$zJ_{xy} = 2J_2^{xy} - 4J_3^{xy} - 2J_4^{xy} + 2\left(J_{l1}^{xy} - J_{l2}^{xy} - J_{l3}^{xy} + J_{l4}^{xy}\right). \tag{9}$$

Since $zJ_{xy} \approx -0.074$ meV, $T_{\rm N}^{\rm MF} = 12.0$ K is close to the observed transition temperature of 12.5 K.

Finally, the xxz spin Hamiltonian and the corresponding exchange parameters are checked by calculating the diffuse scattering near the transition. A magnetic supercell is constructed containing $8 \times 8 \times 8$ chemical unit cells with 4096 Tb ions (eight atoms per chemical unit cell). Using the parameter values in Table I, a forward cluster Monte Carlo simulation [38] is performed just above the transition temperature of $T = 12.5$ K starting with the initial ground-state

configuration. After 1000 Monte Carlo cycles (on average, one cycle visits each of the 4096 atoms once), the diffuse scattering pattern is calculated including the contributions of each of the three domains.

The resulting diffuse scattering pattern reveals significant 3D spin correlations. Figures 3(c) and 3(d) show the calculated diffraction pattern in the $(H, 0, L)$ plane and the line cut along $[0, 0, L]$. The agreement between experiment and theory is excellent: strong streak-like diffuse scattering appears at $H = 2, 4, 8$ but is weak at $H = 6$ and the profile along $(0, 0, L)$ has the same intensity distribution as in the experiment. The peaks that appear at even L are caused by the $\pm 60^\circ$ domains while the peaks at odd L are caused by the 0° domain. Remarkably, the Monte Carlo simulation gives the correct ground state up to the transition temperature.

Monte Carlo simulations also indicate that competing ground states lie close in energy to the state in Figs. 1(c) and 1(d) due to the sizable AF exchange $J_{l2}^{xy} \approx -0.027$ meV between parallel spins. This suggests that doping or pressure might produce a complex phase diagram.

V. FIRST-PRINCIPLES CALCULATIONS

To connect TIG's rather complex physical structure to its observed magnetism, we performed first-principles calculations using the linearized augmented plane-wave density-functional theory code WIEN2K [39]. We employed two standard approximations: the generalized gradient approximation (GGA) and the correlated version of this approach known as GGA + U, in which a Hubbard U (here chosen as 6 eV) is applied to the Tb $4f$ orbitals. To account for potential magnetoelastic effects [40–43], the experimental structure [44] of similar compounds was optimized within the GGA in an assumed FM Tb configuration. Muffin-tin radii of 2.17, 2.4, and 2.5 Bohr were chosen, respectively, for the Ga, Ir, and Tb atoms. Corresponding to the product of the smallest muffin-tin radius and the largest plane-wave expansion wave vector, $RK_{\max}$ was set to 8.0. Given the rather detailed exposition in the previous work [26], we have focused on the interlayer exchange couplings.

Four magnetic states were studied—the previously mentioned FM configuration and three AFM configurations. AF_1 has the 3 Tb-Tb planar neighbors anti-aligned and the next-nearest and next-next-nearest-neighbor planes FM and AFM coupled, respectively; AF_2 has the same planar orientation but next-nearest and next-next-nearest planes AFM and FM coupled; and AF_3 is an interlayer AF state with planar neighbors aligned and next-nearest-neighbor Tb planes anti-aligned. In all cases, the same distorted honeycomb structure with lattice parameters taken from experiment was assumed. The possible ground states given above correspond to a substantially simplified set of configurations compared with the canted state obtained from the neutron-diffraction results, which is closest to AF_2. Nevertheless, it captures important aspects of the relevant physics.

For simplicity, our calculations do not include SOC and so neglect the Tb orbital moments. Using GGA + U, all magnetic states have a substantial Tb spin moment of 6.06 μ_B, slightly larger than the spin moment of 5.83 μ_B obtained using the straight GGA and in good agreement with previous work [26]. Within the GGA + U, AF_1 has the lowest energy, AF_2 and AF_3 lie 13 and 16 meV per Tb higher, respectively, and the FM state lies 43 meV per Tb higher.

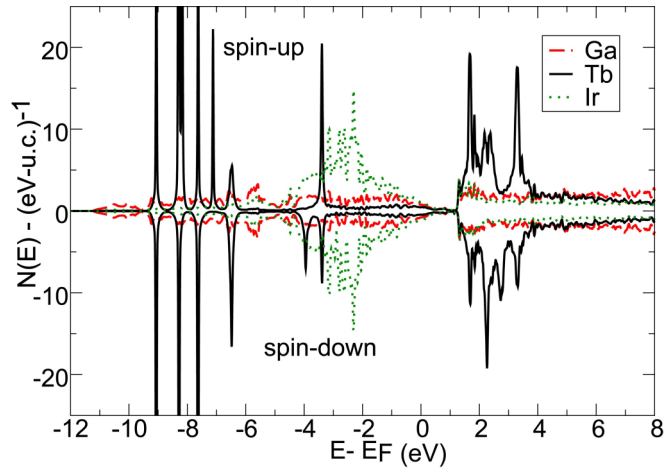

FIG. 6. The calculated density of states of $Tb_2Ir_3Ga_9$ in the AF_1 phase.

These energy differences were mapped onto a simple Heisenberg model including one intralayer nearest-neighbor coupling $J^{(1)}$ and two next-nearest-neighbor and next-next-nearest-neighbor interlayer couplings $J^{(2)}$ and $J^{(3)}$. Using $S(S+1) = 42$, we find $J^{(1)} = -0.22$ meV, $J^{(2)} = -0.02$ meV, and $J^{(3)} = -0.18$ meV—all AFM. Notice that the next-next-nearest-neighbor coupling $J^{(3)}$ is *not* substantially smaller than the nearest-neighbor coupling $J^{(1)}$ despite the larger distances spanned by $J^{(3)}$ (5.37 Å) relative to the distances spanned by the $J^{(1)}$ interactions (4.28 and 4.38 Å). One may directly compare the result for $J^{(1)}$ to that for J_2^{xy} and results for $J^{(2)}$ and $J^{(3)}$ to those for J_{l1}^{xy} and J_{l2}^{xy} in Table I.

Although the distances 5.36 and 5.37 Å spanned by $J^{(2)}$ and $J^{(3)}$ differ by just 0.01 Å, those interactions are substantially different within GGA + U. In agreement with the GGA + U calculation, INS fits find that $|J_{l1}^{xy}| \ll |J_{l2}^{xy}|$. We ascribe the different magnitudes of those exchange couplings obtained from GGA + U and INS to the well-known difficulties experienced by density-functional theory in quantitatively describing $4f$ physics. In any case, we reproduce both the right general size of these interactions and their surprising, yet experimentally validated, slow falloff with distance.

The calculated ground state density-of-states of TIG in Fig. 6 indicates the highly localized character of the Tb $4f$ states along with the more delocalized character of Ir and Ga. As in previous work [26], the density of states is relatively low at the Fermi level, displays a weak gap just above, and then exhibits peaks associated with the unoccupied Tb $4f$ orbitals. The GGA + U approach properly displaces the Tb $4f$ states above and below the Fermi level.

With multiple Ga atoms between the Tb planes, TIG contains several possible indirect exchange or superexchange pathways. Indeed, recent work [45,46] for $3d$ compounds finds that such pathways can produce large exchange in-

teractions even at distances substantially exceeding 5 Å. Despite the typical localization of $4f$ moments, it is possible that the combination of Tb and Ga produces a similar effect.

VI. DISCUSSION AND CONCLUSION

It is well known that the charge distribution of the Tb^{3+} f orbital is highly anisotropic [47]. In our numerical fits to the inelastic spectra, both first-neighbor interactions J_1 and J_{l1} within each layer or between layers are negligible. While J_1 couples sites with $\mathbf{R} = \mathbf{R}_i - \mathbf{R}_j$ along $\mathbf{a}$ ($R = 4.28$ Å), J_{l1} couples sites with $\mathbf{R} \cdot \mathbf{a} = 0$ ($R = 5.33$ Å). This suggests that, for small R, the exchange couplings satisfy

$$J_{ij} \approx \frac{J(R)}{R^4}\{(\mathbf{R}_i - \mathbf{R}_j) \cdot \mathbf{a}(\mathbf{R}_i - \mathbf{R}_j) \cdot \mathbf{b}\}^2. \tag{10}$$

Since the Tb^{3+} orbitals are aligned along $\mathbf{a}$, the exchange couplings both parallel and perpendicular to the axis of the f orbitals are negligible. An exception to this conjecture is the exchange interaction J_{l4}^{xy} ($R = 7.53$ Å). Because this interaction span larger distances than J_1 and J_{l1}, it may involve more complex exchange pathways meditated by Ga ions, as discussed in Sec. V. Although the xy exchange interactions can be FM (J_3^{xy}, J_4^{xy}, and $J_{l3}^{xy} > 0$) or AF (J_2^{xy}, J_{l2}^{xy}, and $J_{l4}^{xy} < 0$), the largest intralayer and interlayer xy exchange couplings J_2^{xy} and J_{l2}^{xy} are both AF, in agreement with the first-principles calculations discussed in the previous section.

Both the inelastic spectra and first-principles calculations indicate that the exchange interactions in TIG are long-ranged. Similar long-ranged interactions extending over many Tb^{3+} layers were found in the compounds $TbNi_2Ge_2$ and $TbNi_2Si_2$, which display several magnetization steps and are possible examples of "devil's staircases" [27,29,48].

Within the Kitaev model [1] on a honeycomb lattice, strong SOC produces a $J_{\text{eff}} = 1/2$ state and the exchange couplings on the three bonds of the nondistorted honeycomb lattice are different. For TIG, the exchange couplings between Tb^{3+} ions in the distorted honeycomb lattice depend on the orientations of the coupled Tb $4f$ orbitals. This bond-dependent exchange is required to understand both the static *and* dynamic properties of TIG.

As in other materials [27,28] containing Tb^{3+} ions, the low-lying crystal-field doublet in TIG affects the λ anomaly of the specific heat [26], which exhibits an $R\ln 2$ entropy characteristic of $J_{\text{eff}} = 1/2$ moments. So there is no doubt that the strong CF potential in TIG splits the $2J + 1 = 13$ levels of Tb^{3+} into a low-lying doublet and 11 higher levels.

Of course, single-ion anisotropy (SIA) should vanish within the low-lying doublet $|\Phi_\pm\rangle$ because $\langle\Phi_\pm|J_\alpha^2|\Phi_\pm\rangle$ is the same for each state. In the absence of easy-axis and easy-plane anisotropies, a rigorous description of TIG must include seven interaction terms per bond [9,34,49]: isotropic Heisenberg exchange J, exchanges J_x and J_z coupling only the x or z spin components, symmetric exchange J_{xy} and antisymmetric (DM) exchange D coupling the x and y spin components, and finally, exchanges J_{zx} and J_{zy} coupling the z and x or y spin components. A complete model of TIG should contain at least five bonds: three bonds to produce the two jumps in the magnetization with field along $\mathbf{a}$ and at least two additional bonds between layers. Adding three g tensor components but constraining the antisymmetric D exchange interactions using the observed canted moment, a rigorous description of TIG then requires *at least* 37 parameters. Needless to say, fitting 37 parameters is nearly impossible and defeats the whole purpose of a model Hamiltonian. Therefore, we have used a phenomenological model containing SIA for general spin S with "only" 13 terms to describe this system. Aside from practicality, another advantage of this model is that the exchange, anisotropy, and $g_{\alpha\alpha}$ components have direct physical interpretations.

The $R_2T_3X_9$ family exhibits a variety of ground states that depend on the competition between long-range magnetic interactions and magneto-crystalline anisotropy arising from the interplay between crystalline electric-field and Kondo effects. Due to the large coordination number (i.e., the rare-earth R has eleven nearest-neighbor X-ligand atoms and six next-nearest-neighbor T-ligand atoms), a slight change in the local environment surrounding the R atom (average bond distance) can lead to drastically different ground states ranging from a mixed-valent to a Kondo-lattice system [17–19,50]. For example, $Dy_2Co_3Al_9$ undergoes transitions into two incommensurate states before locking into a low-temperature commensurate state [15]. This complex phase diagram indicates significant magnetic frustration due to the long-range exchange couplings which also appear in TIG. However, the prevailing easy-plane anisotropy of TIG drives the system into a commensurate spin state, albeit one with many competing states of slightly higher energy.

To summarize, neutron diffraction and INS measurements were used to investigate the static and dynamical properties of the honeycomb-lattice TIG. Neutron-diffraction measurements on a single crystal reveal a canted AFM spin configuration with a moment of about $1.22\mu_B$/f.u. along $\mathbf{b}$. Fits to the inelastic spectrum indicate bond-dependent exchange interactions while Monte Carlo simulations and first-principles calculations suggest competing ground states. Consequently, TIG has a great deal in common with other $J_{\text{eff}} = 1/2$ materials on a honeycomb lattice.

ACKNOWLEDGMENTS

Research at ORNL's HFIR and SNS was sponsored by the Scientific User Facilities Division, Office of Basic Energy Sciences, US Department of Energy (DOE). R.S.F., M.E.M., and D.P. acknowledge support by the US Department of Energy, Office of Basic Energy Sciences, Materials Sciences and Engineering Division. Work in the Materials Science Division at Argonne National Laboratory (crystal growth and magnetic characterization) was supported by the US Department of Energy, Office of Science, Basic Energy Sciences, Materials Science and Engineering Division.

[1] A. Kitaev, Anyons in an exactly solved model and beyond, Ann. Phys. (NY) **321**, 2 (2006).

[2] W. Witczak-Krempa, G. Chen, Y. B. Kim, and L. Balents, Correlated quantum phenomena in the strong

spin-orbit regime, Annu. Rev. Condens. Matter Phys. **5**, 57 (2014).

[3] H. Takagi, T. Takayama, G. Jackeli, G. Khaliullin, and S. E. Nagler, Concept and realization of Kitaev quantum spin liquids, Nat. Rev. Phys. **1**, 264 (2019).

[4] J. Chaloupka, G. Jackeli, and G. Khaliullin, Kitaev-Heisenberg Model on a Honeycomb Lattice: Possible Exotic Phases in Iridium Oxides A_2IrO_3, Phys. Rev. Lett. **105**, 027204 (2010).

[5] K. W. Plumb, J. P. Clancy, L. J. Sandilands, V. V. Shankar, Y. F. Hu, K. S. Burch, H.-Y. Kee, and Y.-J. Kim, α-$RuCl_3$: A spin-orbit assisted Mott insulator on a honeycomb lattice, Phys. Rev. B **90**, 041112(R) (2014).

[6] A. Banerjee, C. A. Bridges, J.-Q. Yan, A. A. Aczel, L. Li, M. B. Stone, G. E. Granroth, M. D. Lumsden, Y. Yiu, J. Knolle, S. Bhattacharjee, D. L. Kovrizhin, R. Moessner, D. A. Tennant, D. G. Mandrus, and S. E. Nagler, Proximate Kitaev quantum spin liquid behaviour in a honeycomb magnet, Nat. Mater. **15**, 733 (2016).

[7] G. Jackeli and G. Khaliullin, Mott Insulators in the Strong Spin-Orbit Coupling Limit: From Heisenberg to a Quantum Compass and Kitaev Models, Phys. Rev. Lett. **102**, 017205 (2009).

[8] Y. Singh, S. Manni, J. Reuther, T. Berlijn, R. Thomale, W. Ku, S. Trebst, and P. Gegenwart, Relevance of the Heisenberg-Kitaev Model for the Honeycomb Lattice Iridates A_2IrO_3, Phys. Rev. Lett. **108**, 127203 (2012).

[9] Y. Li, G. Chen, W. Tong, L. Pi, J. Liu, Z. Yang, X. Wang, and Q. Zhang, Rare-Earth Triangular Lattice Spin Liquid: A Single-Crystal Study of $YbMgGaO_4$, Phys. Rev. Lett. **115**, 167203 (2015).

[10] J. Xing, E. Feng, Y. Liu, E. Emmanouilidou, C. Hu, J. Liu, D. Graf, A. P. Ramirez, G. Chen, H. Cao, and N. Ni, Neel-type antiferromagnetic order and magnetic field–temperature phase diagram in the spin-1/2 rare-earth honeycomb compound $YbCl_3$, Phys. Rev. B **102**, 014427 (2020).

[11] L. Clark, G. Sala, D. D. Maharaj, M. B. Stone, K. S. Knight, M. T. F. Telling, X. Wang, X. Xu, J. Kim, Y. Li, S.-W. Cheong, and B. D. Gaulin, Two-dimensional spin liquid behaviour in the triangular-honeycomb antiferromagnet $TbInO_3$, Nat. Phys. **15**, 262 (2019).

[12] J. Kim, X. Wang, F.-T. Huang, Y. Wang, X. Fang, X. Luo, Y. Li, M. Wu, S. Mori, D. Kwok, E. D. Mun, V. S. Zapf, and S.-W. Cheong, Spin Liquid State and Topological Structural Defects in Hexagonal $TbInO_3$, Phys. Rev. X **9**, 031005 (2019).

[13] Z.-X. Luo and G. Chen, Honeycomb rare-earth magnets with anisotropic exchange interactions, SciPost Phys. Core **3**, 004 (2020).

[14] S.-H. Jang, R. Sano, Y. Kato, and Y. Motome, Antiferromagnetic Kitaev interaction in f-electron based honeycomb magnets, Phys. Rev. B **99**, 241106(R) (2019).

[15] D. I. Gorbunov, M. S. Henriques, N. Qureshi, B. Ouladdiaf, C. S. Mejía, J. Gronemann, A. V. Andreev, V. Petříček, E. L. Green, and J. Wosnitza, Spontaneous and field-induced magnetic phase transitions in $Dy_2Co_3Al_9$: Effects of exchange frustration, Phys. Rev. Mater. **2**, 084406 (2018).

[16] R. A. Gordon, F. J. DiSalvo, R. Pöttgen, and N. E. Brese, Crystal structure, electric and magnetic behaviour of $Ce_2Pd_9Sb_3$, J. Chem. Soc., Faraday Trans. **92**, 2167 (1996).

[17] S. K. Dhar, C. Mitra, P. Manfrinetti, A. Palenzona, and P. Bonville, Magnetic behaviour of $Yb_2Co_3T_9$ (T = Ga and Al), Phys. B **259-261**, 150 (1999).

[18] O. Trovarelli, C. Geibel, B. Buschinger, R. Borth, S. Mederle, M. Grosche, G. Sparn, F. Steglich, O. Brosch, and L. Donnevert, Magnetic, transport, and thermal properties of $Yb_2T_3X_9$ compounds (T = Rh, Ir; X = Al, Ga), Phys. Rev. B **60**, 1136 (1999).

[19] T. Okane, S.-I. Fujimori, A. Ino, A. Fujimori, S. K. Dhar, C. Mitra, P. Manfrinetti, A. Palenzona, and O. Sakai, Photoemission study of $Yb_2Co_3X_9$: variation of the electronic structure from a mixed-valent to Kondo-lattice system, Phys. Rev. B **65**, 125102 (2002).

[20] R. Troć, O. Tougait, and H. Noël, Crystal structure and properties of $U_2Co_3Al_9$, Intermetallics **15**, 1091 (2007).

[21] R. E. Gladyshevskii, K. Cenzual, and E. Parthé, $Y_2Co_3Al_9$ with $Y_2Co_3Ga_9$ type structure: An intergrowth of CsCl- and Th_3Pd_5-type slabs, J. Alloys Compd. **182**, 165 (1992).

[22] M. Schlüter and W. Jeitschko, Rare earth metal ruthenium Gallides $R_2Ru_3Ga_9$ with $Y_2Co_3Ga_9$ type structure, Z. Anorg. Allg. Chem. **626**, 2217 (2000).

[23] Y. Lutsyshyn, Y. Tokaychuk, and R. Gladyshevskii, Rare-earth cobalt aluminides with $Y_2Co_3Ga_9$-type structure, Chem. Met. Alloys **4**, 243 (2011).

[24] H. R. Molavian, M. J. P. Gingras, and B. Canals, Dynamically Induced Frustration as a Route to a Quantum Spin Ice State in $Tb_2Ti_2O_7$ Via Virtual Crystal Field Excitations and Quantum Many-Body Effects, Phys. Rev. Lett. **98**, 157204 (2007).

[25] S. H. Curnoe, Effective spin-1/2 exchange model for $Tb_2Ti_2O_7$, Phys. Rev. B **88**, 014429 (2013).

[26] M. A. Khan, Q. Zhang, J.-K. Bao, R. S. Fishman, A. S. Botana, Y. Choi, G. Fabbris, D. Haskel, J. Singleton, and J. F. Mitchell, Steplike metamagnetic transitions in a honeycomb lattice antiferromagnet $Tb_2Ir_3Ga_9$, Phys. Rev. Mater. **3**, 114411 (2019).

[27] S. Bud'ko, Z. Islam, T. Wiener, I. Fisher, A. Lacerda, and P. Canfield, Anisotropy and metamagnetism in the RNi_2Ge_2 (R = Y, La-Nd, Sm-Lu) series, J. Magn. Magn. Mater. **205**, 53 (1999).

[28] T. A. Wiener, I. R. Fisher, S. L. Bud'ko, A. Kracher, and P. C. Canfield, Design of a metallic Ising spin glass in the $Y_{1-x}Tb_xNi_2Ge_2$ system, Phys. Rev. B **62**, 15056 (2000).

[29] T. Shigeoka, H. Fujii, M. Nishi, Y. Uwatoko, T. Takabatake, I. Oguro, K. Motoya, N. Iwata, and Y. Ito, Metamagnetism in $TbNi_2Si_2$ single crystal, J. Phys. Soc. Jpn. **61**, 4559 (1992).

[30] F. Ye, Y. Liu, R. Whitfield, R. Osborn, and S. Rosenkranz, Implementation of cross correlation for energy discrimination on the time-of-flight spectrometer CORELLI, J. Appl. Crystallogr. **51**, 315 (2018).

[31] See Supplemental Material at http://link.aps.org/supplemental/10.1103/PhysRevB.103.184413 for further details of symmetry analysis, sample characterization, and the spin wave calculation at field at 7 T.

[32] P. A. Maksimov and A. L. Chernyshev, Field-induced dynamical properties of the XXZ model on a honeycomb lattice, Phys. Rev. B **93**, 014418 (2016).

[33] H. S. Nair, J. M. Brown, E. Coldren, G. Hester, M. P. Gelfand, A. Podlesnyak, Q. Huang, and K. A. Ross, Short-range order in the quantum xxz honeycomb lattice material $BaCo_2(PO_4)_2$, Phys. Rev. B **97**, 134409 (2018).

[34] T. Matsumoto and S. Hayami, Nonreciprocal magnons due to symmetric anisotropic exchange interaction in honeycomb antiferromagnets, Phys. Rev. B **101**, 224419 (2020).

[35] A. R. Mackintosh and H. Møller, Spin waves, in *Magnetic Properties of Rare Earth Metals*, edited by R. J. Elliott (Plenum Press, New York, 1972), Chap. 5.

[36] R. S. Fishman, J. A. Fernandez-Baca, and T. Rõõm, *Spin-Wave Theory and its Applications to Neutron Scattering and THz Spectroscopy* (IOP Concise Physics, Morgan and Claypool Publishers, San Rafael, 2018).

[37] J. J. Rhyne, S. Foner, E. J. McNiff, and R. Doclo, Rare earth metal single crystals. I. high-field properties of Dy, Er, Ho, Tb, and Gd, J. Appl. Phys. **39**, 892 (1968).

[38] M. D'Onorio De Meo and S. K. Oh, Wolff algorithm and anisotropic continuous-spin models: An application to the spin-van der Waals model, Phys. Rev. B **46**, 257 (1992).

[39] P. Blaha, K. Schwarz, G. K. Madsen, D. Kvasnicka, J. Luitz, R. Loskowsk, and F. Tran, WIEN2K, An Augmented Plane Wave + Local Orbitals Program for Calculating Crystal Properties (Institut Für Physikalische und Theoretische Chemie Vienna, Austria, 2001).

[40] G. Pokharel, A. May, D. Parker, S. Calder, G. Ehlers, A. Huq, S. Kimber, H. S. Arachchige, L. Poudel, M. McGuire, D. Mandrus, and A. Christianson, Negative thermal expansion and magnetoelastic coupling in the breathing pyrochlore lattice material $LiGaCr_4S_8$, Phys. Rev. B **97**, 134117 (2018).

[41] L. D. Sanjeewa, J. Xing, K. Taddei, D. Parker, R. Custelcean, C. dela Cruz, and A. S. Sefat, Evidence of Ba-substitution induced spin-canting in the magnetic Weyl semimetal $EuCd_2As_2$, Phys. Rev. B **102**, 104404 (2020).

[42] J.-Q. Yan, Y. Liu, D. S. Parker, Y. Wu, A. Aczel, M. Matsuda, M. A. McGuire, and B. C. Sales, A-type antiferromagnetic order in $MnBi_4Te_7$ and $MnBi_6Te_{10}$ single crystals, Phys. Rev. Mater. **4**, 054202 (2020).

[43] K. Chen, B. Wang, J.-Q. Yan, D. Parker, J.-S. Zhou, Y. Uwatoko, and J.-G. Cheng, Suppression of the antiferromagnetic metallic state in the pressurized $MnBi_2Te_4$ single crystal, Phys. Rev. Mater. **3**, 094201 (2019).

[44] Y. Grin and P. Rogl, Phases with the $Y_2Co_3Ga_9$ type structure in rare earth metal–rhodium (iridium)–gallium systems, Inorg. Mater. (USSR) **25**, 514 (1989).

[45] T. Williams, A. Taylor, A. Christianson, S. Hahn, R. Fishman, D. Parker, M. McGuire, B. Sales, and M. Lumsden, Extended magnetic exchange interactions in the high-temperature ferromagnet MnBi, Appl. Phys. Lett. **108**, 192403 (2016).

[46] N. Sirica, P. Vilmercati, F. Bondino, I. Pis, S. Nappini, S.-K. Mo, A. V. Fedorov, P. K. Das, I. Vobornik, J. Fujii, L. Li, D. Sapkota, D. Parker, D. Mandrus, and N. Mannella, The nature of ferromagnetism in the chiral helimagnet $Cr_{1/3}NbS_2$, Commun. Phys. **3**, 83 (2020).

[47] J. Rhyne, Bulk magnetic properties, in *Magnetic Properties of Rare Earth Metals*, edited by R. J. Elliott (Plenum Press, New York, 1972), Chap. 4.

[48] J. Blanco, D. Gignoux, D. Schmitt, and C. Vettier, Field induced magnetic structures in $TbNi_2Si_2$, J. Magn. Magn. Mater. **97**, 4 (1991).

[49] P. A. Maksimov, Z. Zhu, S. R. White, and A. L. Chernyshev, Anisotropic-Exchange Magnets on a Triangular Lattice: Spin Waves, Accidental Degeneracies, and Dual Spin Liquids, Phys. Rev. X **9**, 021017 (2019).

[50] J. Niermann, B. Fehrmann, M. W. Wolff, and W. Jeitschko, Preparation and crystal structure of ternary rare-earth platinum metal aluminides $R_2T_3Al_9$ (T = Rh, Ir, Pd) with $Y_2Co_3Ga_9$-type structure and magnetic properties of the iridium compounds, J. Solid State Chem. **177**, 2600 (2004).